Publisher: GSA
Journal: GEOL: Geology
DOI:10.1130/G46516.1

Fault reactivation and strain partitioning across the brittle-ductile transition

Gabriel G. Meyer, Nicolas Brantut, Thomas M. Mitchell, and Philip G. Meredith

*Department of Earth Sciences, University College London, London, UK****[[Postal code?]]***

ABSTRACT

The so-called "brittle-ductile transition" is thought to be the strongest part of the lithosphere, and defines the lower limit of the seismogenic zone. It is characterized not only by a transition from localized to distributed (ductile) deformation, but also by a gradual change in microscale deformation mechanism, from microcracking to crystal plasticity. These two transitions can occur separately under different conditions. The threshold conditions bounding the transitions are expected to control how deformation is partitioned between localized fault slip and bulk ductile deformation. Here, we report results from triaxial deformation experiments on pre-faulted cores of Carrara marble over a range of confining pressures, and determine the relative partitioning of the total deformation between bulk strain and on-fault slip. We find that the transition initiates when fault strength (σ_f) exceeds the yield stress (σ_y) of the bulk rock, and terminates when it exceeds its ductile flow stress (σ_{flow}). In this domain, yield in the bulk**[[bulk rock?]]** occurs first, and fault slip is reactivated as a result of bulk strain hardening. The contribution of fault slip to the total deformation is proportional to the ratio (σ_f – σ_y)/(σ_{flow} – σ_y). We propose an updated crustal strength profile extending the localized-ductile transition toward shallower regions where the strength of the crust would be

limited by fault friction, but significant proportions of tectonic deformation could be accommodated simultaneously by distributed ductile flow.

INTRODUCTION AND METHODOLOGY

Under the low pressure and temperature conditions of the upper crust, rocks generally deform by grain-scale microcracking, and crustal-scale deformation is accommodated by slip on discrete fault planes. In this regime, the overall strength of the crust is limited by fault friction (Scholz, 2002; Paterson and Wong, 2005). Deeper in the crust, at higher pressure and temperature, rock deformation becomes more diffuse, and may be driven by crystal plastic phenomena such as dislocation creep. Here, the overall strength of rocks can generally be described by a steady-state flow law sensitive primarily to temperature and strain rate (e.g., Goetze and Brace, 1972; Evans and Kohlstedt, 1995). The transition between these two rheological domains, the so-called “brittle-ductile transition”, occurs over a pressure and temperature range where rocks deform by an interplay of cracking and crystal plasticity. The brittle-ductile transition commonly loosely refers to the progressive change in crustal rheology with increasing depth; here we will use the term “ductile” in the sense described by Rutter (1986), whereby it refers to macroscale distributed flow, regardless of the nature of the deformation mechanism, and will use “brittle” to describe fracturing processes at all scales.

In nature, the brittle-ductile transition zone has been identified in exhumed shear zones showing markers of crystal plasticity (e.g., mylonites) overprinted by slip planes and pseudotachylytes that are inherent to the brittle regime (e.g., Sibson, 1980; Passchier, 1982; Hobbs et al., 1986). Such field evidence suggests that the transition in deformation mechanism is associated with a change in the degree of strain localization, from narrow frictional slip zones to wider plastic shear zones.

Laboratory experiments have shown that the transition from localized fracture to ductile flow generally occurs when the frictional strength of the fault, σ_f, equals **[[or exceeds?]]** the bulk flow stress of the rock, σ_{flow} (Byerlee, 1968; Kohlstedt et al., 1995). However, distributed deformation at the macroscopic scale may still be dominated by brittle microscale processes, and only further increases in pressure and temperature lead to fully crystal-plastic flow. This shows that the macroscale transition in strain localization (localized-ductile transition) is not necessarily the same as the microscale transition in deformation mechanism (brittle-plastic transition) and that the two transitions can occur under different pressure and temperature conditions. The resulting complex interplay between brittle and plastic mechanisms makes the flow stress σ_{flow} sensitive to a large number of parameters in the ductile regime (see Evans et al., 1995**[[Evans et al., 1995 is not in the reference list]]**, and references therein), notably the imposed strain rate and the accumulated strain.

Furthermore, the criterion $\sigma_{flow} > \sigma_f$ for the onset of ductile deformation was originally established from studies on initially intact materials undergoing a simple monotonic loading history, and describes deformation regimes in a binary manner (localized or distributed) without emphasizing the potential for coexistence of both fault slip and bulk ductile flow. The applicability of this criterion to the crust might therefore be limited, because crustal-scale deformation is controlled by preexisting structures (faults and shear zones; see, e.g., Goetze and Evans, 1979; Brace and Kohlstedt, 1980). Thus, it remains unclear if and how faults are reactivated across the brittle-ductile transition. Previous experimental studies have commonly used sample geometries that enforce sliding on narrow shear zones between essentially rigid blocks under increasing pressure and temperature conditions (e.g., Shimamoto, 1986; Pec et al., 2016), which do not allow for quantification of partitioning between fault slip and bulk strain.

Here, we conducted rock deformation experiments on pre-faulted samples of Carrara marble and monitored strain partitioning and fault reactivation across the localized-ductile transition. Our experiments were performed at room temperature and confining pressures (P_c) from 5 to 80 MPa. We determined partitioning of the total shortening between fault slip and off-fault matrix strain by subtracting the matrix strain (measured with strain gauges) from the total shortening (measured with external displacement transducers).

Experiments were conducted in two stages. During the first stage, samples were pre-faulted by loading at $P_c = 5$ MPa until localized brittle failure occurred. Following failure, an additional increment of shortening $\Delta L/L$ (L—length) of either 0.1% or 1% was allowed to accumulate before proceeding to the second stage, in order to test any effect of accumulated fault slip on the transition. In the second stage, P_c was increased stepwise from 5 to 80 MPa in 5 or 10 MPa increments. At each pressure step, the samples were reloaded at an axial shortening rate of $\dot{\varepsilon} = 10^{-5}$ s^{-1}**[[Should the units for shortening rate include a length unit (all instances)? If not, briefly explain how this is normalized]]** unshortil 0.1% of irrecoverable axial shortening was accumulated, and then unloaded before proceeding to the next pressure step (see Section DR1 and Fig. DR2 in the GSA Data Repository[1] for an extended methodology, and Table DR3 for a summary of experimental conditions).

RESULTS

During the first stage (Fig. 1), the sample behaves in a manner typical of the brittle regime, and the stress drop (accompanied by partial relaxation of the off-fault elastic strain) marks the formation of the macroscopic shear fault. During the second stage, at each confining pressure step, the stress-shortening relationship is initially linear, but deviates from linearity at some threshold stress σ_y, and then tends to plateau (Fig. 1A). This “plateau” stress increases significantly with increasing P_c. At low P_c (10 and 20 MPa), the matrix strain (ε_{matrix}) initially increases at the same rate as the total shortening ($\Delta L/L$), then deviates toward a constant value. The deviation point occurs at a stress denoted σ_f, and marks the onset of fault slip (triangles in Fig. 1B). At intermediate P_c (30–60 MPa), the same deviation is observed to occur, but ε_{matrix} continues to increase beyond this point, albeit at a lower rate, indicating contributions from both matrix strain and fault slip to the total shortening. This observation appears to be independent of shortening, as demonstrated in an additional experiment where a single, second-stage deformation cycle was performed at $P_c = 35$ MPa, which shows no further deviation in matrix strain for a total shortening of up to a further 2% (Fig. DR4). Finally, at the highest P_c (70 MPa and above), ε_{matrix} remains equal to $\Delta L/L$ throughout the deformation cycle, which implies that the fault is fully locked.

To assess the extent of microcracking in the matrix, we measured the horizontal P-wave speed across the fault during each deformation cycle (Fig. DR5). The wave speed at the start of each cycle increased with confining pressure. During deformation, the wave speed changed very little for cycles at P_c <30 MPa, but decreased progressively for all cycles at higher pressures. The magnitude of the decrease in P-wave speed increased with increasing P_c from 30 to 60 MPa but then decreased at higher confinement.

At $P_c = 10$ and 20 MPa, the yield stress and the fault strength are equal, and the calculated slip contributes close to 100% of the total shortening (Figs. 2A and 2D). Between $P_c = 30$ MPa and $P_c = 60$ MPa, σ_f increases linearly with P_c, whereas σ_y remains approximately constant at ~115 MPa. Over this pressure range, the slip contribution progressively decreases from ~80% at $P_c = 30$ MPa down to ~15% at $P_c =$ 60 MPa. At $P_c = 70$ MPa and above, the fault is fully locked, σ_f becomes inaccessible, and the slip contribution drops to zero. During the experiment where more slip is accumulated on the fault (1% rather than 0.1%) prior to stage 2 (Figs. 2B and 2E), σ_f and σ_y behave in a comparable manner to that described above, but σ_f increases with increasing P_c at a slightly higher rate. As a result, the deviation between the two initiates at $P_c = 20$ MPa and the fault becomes fully locked around $P_c = 55$ MPa. Similarly, the slip contribution decreases from >60% at $P_c = 20$ MPa to 20% at $P_c = 45$ MPa. During the experiment at the higher shortening rate of 10^{-4} s^{-1} (Figs. 2C and 2F), the trend remains the same, but the P_c domain over which $\sigma_f = \sigma_y$ extends up to 35 MPa. From P_c = 40 MPa to $P_c = 60$ MPa, σ_f continues to increase linearly with increasing P_c, and σ_y remains approximately constant at 135 MPa. The slip contribution decreases from ~80% at $P_c = 40$ MPa to 0% at $P_c = 60$ MPa. At the lower shortening rate of 10^{-6} s^{-1}, the stress at the onset of fault slip σ_f does not differ significantly from that at higher shortening rates. By contrast with the test performed at 10^{-4} s^{-1}, where the decrease in slip contribution initiates at $P_c \approx 40$ MPa, at the lower rate of 10^{-6} s^{-1}, that decrease initiates at $P_c \approx 15$ MPa.

DISCUSSION AND CONCLUSION

Our results show that with increasing confining pressure, faulted Carrara marble samples gradually shift from purely localized behavior where most of the deformation is accommodated by slip on the fault, to ductile behavior where strain is homogeneously distributed throughout the sample and the fault is locked. The transition commences at the confining pressure where fault strength becomes larger than matrix yield stress ($\sigma_f > \sigma_y$), and terminates when fault strength becomes equal to matrix flow stress ($\sigma_f = \sigma_{flow}$) (Figs. 1A, 1B, and 1C**[[Fig. 1 does not have a panel C – should this be Fig. 2?]]**). Thus, a transitional behavior where both fault slip and matrix deformation coexist occurs over a range of conditions delimited by $\sigma_y < \sigma_f < \sigma_{flow}$.

When $\sigma_f = \sigma_y$, no matrix strain is recorded (confirmed by the absence of significant variations in P-wave speed), and the yield stress of the rock is controlled by fault friction alone. This can be explained by the fact that, at low P_c, the fault frictional strength is likely lower than the yield stress of the off-fault matrix material (Fredrich et al., 1989). However, when $\sigma_f > \sigma_y$, the rock initially yields in the matrix and deformation is entirely ductile. The associated decrease in P-wave speed indicates that this ductility is driven mostly by diffuse microcracking. However, upon further loading, strain hardening eventually leads to reactivation of the fault when the applied stress reaches σ_f (confirmed by the existence of a single fault plane in post-mortem samples; Figs. DR6 and DR7). After reactivation, both ductile matrix strain and fault slip operate simultaneously, and partitioning of the total shortening between them is proportional to the ratio $(\sigma_f - \sigma_y)/(\sigma_{flow} - \sigma_y)$, regardless of shortening rate and initial fault slip (Fig. 3). When $\sigma_f \geq \sigma_{flow}$, the fault is locked and the deformation is fully ductile. The decrease in magnitude of the drop in P-wave speed under these conditions suggests that the contribution of microcracking to the overall deformation decreases with respect to that of crystal plasticity (Fredrich et al., 1989).

Our observations highlight the key role of the yield stress in the partitioning between localized fault slip and bulk deformation of the matrix. In Carrara marble, the control on yield stress switches from microcracking to crystal plasticity at low P_c (~50 MPa; Fredrich et al., 1989; Fig. 4). This is corroborated by the pressure-insensitive behavior exhibited by our yield stress data at P_c >40 MPa (Figs. 2A–2C). Remarkably, the impact of rate**[[Rate of what?]]** on the partitioning of deformation is well captured, to first order, by the rate dependency of yield stress only (Fig. 3).

Our results are compatible with those of previous studies on silicate rocks using initially intact samples, where a similar progression from initial ductile yielding to strain localization and faulting with increasing deformation has been reported for conditions approaching the brittle-ductile transition (Hirth and Tullis, 1994). Additionally, the coexistence of ductile flow and localized shear zones has been observed in granite and feldspar aggregates (Tullis and Yund, 1977, 1992).

The existence of a zone of transitional behavior delimited by the yield stress can be integrated into a crustal-strength profile model (e.g., Kirby, 1980; Brace and Kohlstedt, 1980; Sibson, 1983; Fig. 4). Because yield stress is systematically lower than the flow stress, it appears that the transitional regime where ductile and localized strain coexist extends toward shallower depths compared to previous models of the brittle-ductile transition, into a depth range usually considered to be fully localized. In this zone, crustal strength is still controlled by fault friction, but with increasing depth, a growing proportion of the strain can be accommodated off-fault as the yield stress diverges from the frictional strength. This would suggest an overall widening of the shear zone, which is consistent with geological (e.g., Sibson, 1977; Scholz, 1988; Shimamoto, 1989; Cooper et al., 2010, 2017) and geophysical (e.g., Cowie et al., 2013) observations. Furthermore, high strain rates during seismic and post-seismic slip would increase both yield and flow stresses, therefore shifting the transition zone to greater depth. This is consistent with the existence of a zone of alternating behavior as discussed by Scholz (1988) and the formation of complex overprinted brittle and ductile structures observed in nature (e.g., Sibson, 1980; Melosh et al., 2014). Conversely, lower strain rates during the interseismic period (10^{-12} s^{-1} to 10^{-15} s^{-1}) would reduce yield and flow stresses, which would in turn promote ductile deformation by shifting the transition zone to shallower depths. In this region of the crust, fault reactivation is dependent on the ability of the crust to harden with increasing strain. If recovery mechanisms are active, it is possible that large amounts of tectonic strain can be accommodated off-fault during transient deformation episodes, and if recovery is predominant, fault reactivation never occurs. Therefore, the gray area in Figure 4 represents all possible stress states in the crust. This rheology could explain the abnormally low stresses recorded around major faults (e.g., Behr and Platt, 2014), but the mechanisms responsible for low-temperature strain hardening and recovery are, to date, mostly unknown.

Unfortunately, there is a paucity of systematic data on low-temperature yield stress in crustal rocks. However, laboratory studies on wet quartz single crystals (e.g., Balderman, 1974; Doukhan and Trépied, 1985) suggest low-temperature yield stresses on the order of 50–100 MPa, which would imply a transition zone depth of only a few kilometers in continental crust.

ACKNOWLEDGMENTS

We thank Whitney Behr, Matej Pec, and Nicola De Paola for their constructive reviews. This project received funding from the European Union's Horizon 2020 research and innovation program under the Marie Sklodowska-Curie grant agreement 642029–ITN CREEP, and under the European Research Council grant agreement 804685–RockDEaF.

REFERENCES CITED

Balderman, M.A., 1974, The effect of strain rate and temperature on the yield point of hydrolytically weakened synthetic quartz: Journal of Geophysical Research, v. 79, p. 1647–1652, https://doi.org/10.1029/JB079i011p01647.

Behr, W.M., and Platt, J.P., 2014, Brittle faults are weak, yet the ductile middle crust is strong: Implications for lithospheric mechanics: Geophysical Research Letters, v. 41, p. 8067–8075, https://doi.org/10.1002/2014GL061349.

Brace, W.F., and Kohlstedt, D.L., 1980, Limits on lithospheric stress imposed by laboratory experiments: Journal of Geophysical Research, v. 85, p. 6248–6252, https://doi.org/10.1029/JB085iB11p06248.

Byerlee, J.D., 1968, Brittle-ductile transition in rocks: Journal of Geophysical Research, v. 73, p. 4741–4750, https://doi.org/10.1029/JB073i014p04741.

Cooper, F.J., Platt, J.P., Platzman, E.S., Grove, M.J., and Seward, G., 2010, Opposing shear senses in a subdetachment mylonite zone: Implications for core complex mechanics: Tectonics, v. 29, TC4019, https://doi.org/10.1029/2009TC002632.

Cooper, F.J., Platt, J.P., and Behr, W.M., 2017, Rheological transitions in the middle crust: Insights from Cordilleran metamorphic core complexes: Solid Earth, v. 8, p. 199–215, https://doi.org/10.5194/se-8-199-2017.

Cowie, P.A., Scholz, C.H., Roberts, G.P., Faure Walker, J.P., and Steer, P., 2013, Viscous roots of active seismogenic faults revealed by geologic slip rate variations: Nature Geoscience, v. 6, p. 1036–1040, https://doi.org/10.1038/ngeo1991.

Doukhan, J.-C., and Trépied, L., 1985, Plastic deformation of quartz single crystals: Bulletin de Minéralogie, v. 108, p. 97–123, https://doi.org/10.3406/bulmi.1985.7860.

Evans, B., and Kohlstedt, D.L., 1995, Rheology of rocks, *in* Ahrens, T.J., ed., Rock Physics and Phase Relations: A Handbook of Physical Constants: American Geophysical Union Reference Shelf 3, p. 148–165.

Fredrich, J.T., Evans, B., and Wong, T.-F., 1989, Micromechanics of the brittle to plastic transition in Carrara marble: Journal of Geophysical Research, v. 94, p. 4129–4145, https://doi.org/10.1029/JB094iB04p04129.

Goetze, C., and Brace, W.F., 1972, Laboratory observations of high-temperature rheology of rocks: Tectonophysics, v. 13, p. 583–600, https://doi.org/10.1016/0040-1951(72)90039-X.

Goetze, C., and Evans, B., 1979, Stress and temperature in the bending lithosphere as constrained by experimental rock mechanics: Geophysical Journal International, v. 59, p. 463–478, https://doi.org/10.1111/j.1365-246X.1979.tb02567.x.

Hirth, G., and Tullis, J., 1994, The brittle-plastic transition in experimentally deformed quartz aggregates: Journal of Geophysical Research, v. 99, p. 11,731–11,747, https://doi.org/10.1029/93JB02873.

Hobbs, B.E., Ord, A., and Teyssier, C., 1986, Earthquakes in the ductile regime?: Pure and Applied Geophysics, v. 124, p. 309–336, https://doi.org/10.1007/BF00875730.

Kirby, S.H., 1980, Tectonic stresses in the lithosphere: Constraints provided by the experimental deformation of rocks: Journal of Geophysical Research, v. 85, p. 6353–6363, https://doi.org/10.1029/JB085iB11p06353.

Kohlstedt, D.L., Evans, B., and Mackwell, S.J., 1995, Strength of the lithosphere: Constraints imposed by laboratory experiments: Journal of Geophysical Research, v. 100, p. 17,587–17,602, https://doi.org/10.1029/95JB01460.

Melosh, B.L., Rowe, C.D., Smit, L., Groenewald, C., Lambert, C.W., and Macey, P., 2014, Snap, Crackle, Pop: Dilational fault breccias record seismic slip below the brittle-plastic transition: Earth and Planetary Science Letters, v. 403, p. 432–445, https://doi.org/10.1016/j.epsl.2014.07.002.

Passchier, C.W., 1982, Pseudotachylyte and the development of ultramylonite bands in the Saint-Barthélemy Massif, French Pyrenees: Journal of Structural Geology, v. 4, p. 69–79, https://doi.org/10.1016/0191-8141(82)90008-6.

[[City of publication?]]Paterson, M.S., and Wong, T.-F., 2005, Experimental Rock Deformation—The Brittle Field: Springer Science & Business Media, 348 p.

Pec, M., Stünitz, H., Heilbronner, R., and Drury, M., 2016, Semi-brittle flow of granitoid fault rocks in experiments: Journal of Geophysical Research: Solid Earth, v. 121, p. 1677–1705, https://doi.org/10.1002/2015JB012513.

Rutter, E.H., 1986, On the nomenclature of mode of failure transitions in rocks: Tectonophysics, v. 122, p. 381–387, https://doi.org/10.1016/0040-1951(86)90153-8.

Scholz, C.H., 1988, The brittle-plastic transition and the depth of seismic faulting: Geologische Rundschau, v. 77, p. 319–328, https://doi.org/10.1007/BF01848693.

Scholz, C.H., 2002, The Mechanics of Earthquakes and Faulting (second edition): Cambridge, UK, Cambridge University Press, 471 p., https://doi.org/10.1017/CBO9780511818516.

Shimamoto, T., 1986, Transition between frictional slip and ductile flow for halite shear zones at room temperature: Science, v. 231, p. 711–714, https://doi.org/10.1126/science.231.4739.711.

Shimamoto, T., 1989, The origin of *S-C* mylonites and a new fault-zone model: Journal of Structural Geology, v. 11, p. 51–64, https://doi.org/10.1016/0191-8141(89)90035-7.

Sibson, R.H., 1977, Fault rocks and fault mechanisms: Journal of the Geological Society, v. 133, p. 191–213, https://doi.org/10.1144/gsjgs.133.3.0191.

Sibson, R.H., 1980, Transient discontinuities in ductile shear zones: Journal of Structural Geology, v. 2, p. 165–171, https://doi.org/10.1016/0191-8141(80)90047-4.

Sibson, R.H., 1983, Continental fault structure and the shallow earthquake source: Journal of the Geological Society, v. 140, p. 741–767, https://doi.org/10.1144/gsjgs.140.5.0741.

Tullis, J., and Yund, R.A., 1977, Experimental deformation of dry Westerly granite: Journal of Geophysical Research, v. 82, p. 5705–5718, https://doi.org/10.1029/JB082i036p05705.

Tullis, J., and Yund, R., 1992, The brittle-ductile transition in feldspar aggregates: An experimental study, *in* Evans, B. and Wong, T.-F., eds., Fault Mechanics and

Transport Properties of Rocks: A Festschrift in Honor of W. F. Brace: New York, Academic Press, International Geophysics, v. 51, p. 89–117, https://doi.org/10.1016/S0074-6142(08)62816-8.

FIGURE CAPTIONS

Figure 1. Mechanical data for full fault reactivation experiment (1% accumulated slip, axial shortening rate $\dot{\varepsilon} = 10^{-5}\ s^{-1}$). A: Differential stress against total axial shortening. B: Matrix strain against total axial shortening. Unloading phases of each cycle have been removed to aid clarity. Squares represent point at which sample yields, and triangles represent point at which the fault in the sample is reactivated (i.e., begins to slip). Numbers above curves represent confining pressure (P_c, in MPa). Inset in B shows the two different recorded deformations.**[[Clarify what is shown in the panel B inset – is this a diagram of the experiment setup? Cross-sectional or plan view? What is the diagonal line? Also explain the triangular diagram at the lower-right corner of panel B]]**

[[In the figure, in axis descriptions, enclose units in parentheses rather than square brackets; italicize “*P*” in “*P*$_c$”]]

Figure 2. A–C: Flow stress (σ_{flow}), maximum stress (σ_{max}), fault strength (σ_f), and yield stress (σ_y) for experiments at varying confining pressure. D–F: Slip contribution to the total shortening during each deformation cycle for experiments at varying confining pressure. Data represent three different scenarios: panels A and D, 0.1% imposed accumulated fault slip and axial shortening rate $\dot{\varepsilon} = 10^{-5}\ s^{-1}$; panels B and E, 1% imposed

accumulated fault slip and $\dot{\varepsilon} = 10^{-5}$ s^{-1}; and panels C and F, 0.1% imposed accumulated fault slip and $\dot{\varepsilon} = 10^{-4}$ s^{-1} (open symbols) and 10^{-6} s^{-1} (solid symbols).

[[In the figure, in axis descriptions, enclose units in parentheses rather than square brackets]]

Figure 3. Slip contribution to total shortening as function of the ratio $(\sigma_f - \sigma_y)/(\sigma_{flow} - \sigma_y)$. Each set of symbols represents different experimental conditions: circles, 0.1% accumulated slip and axial shortening rate $\dot{\varepsilon} = 10^{-5}$ s^{-1}; triangles, 1% accumulated slip and $\dot{\varepsilon} = 10^{-5}$ s^{-1}; and stars, 0.1% accumulated slip and $\dot{\varepsilon} = 10^{-4}$ s^{-1}.

[[In the figure, in axis descriptions, enclose units in parentheses rather than square brackets; remove italics from all instances of "σ"]]

Figure 4. Conceptual model of crustal strength. Bold line represents strength profile, and gray area, possible stress states in crust.**[[Explain what the last column describes, and what the downward-pointing arrows indicate in the rightmost two columns]]** Loc.—localized deformation; Distrib.—distributed (ductile) deformation; Crys.—crystal.

[[In the figure, delete the spaces surrounding the hyphens in "Semibrittle-plastic" and "Localized-ductile"]]

[1] GSA Data Repository item 2019xxx, extended methodology (Section DR1), sample pictures (Fig. DR2), summary of the experimental conditions (Table DR3), mechanical data for single-cycle experiment (Fig. DR4), P-wave speed data (Fig. DR5), post-mortem sample picture (Fig. DR6), and slip proportion measurements (Fig. DR7), is available

online at http://www.geosociety.org/datarepository/2019/, or on request from editing@geosociety.org.

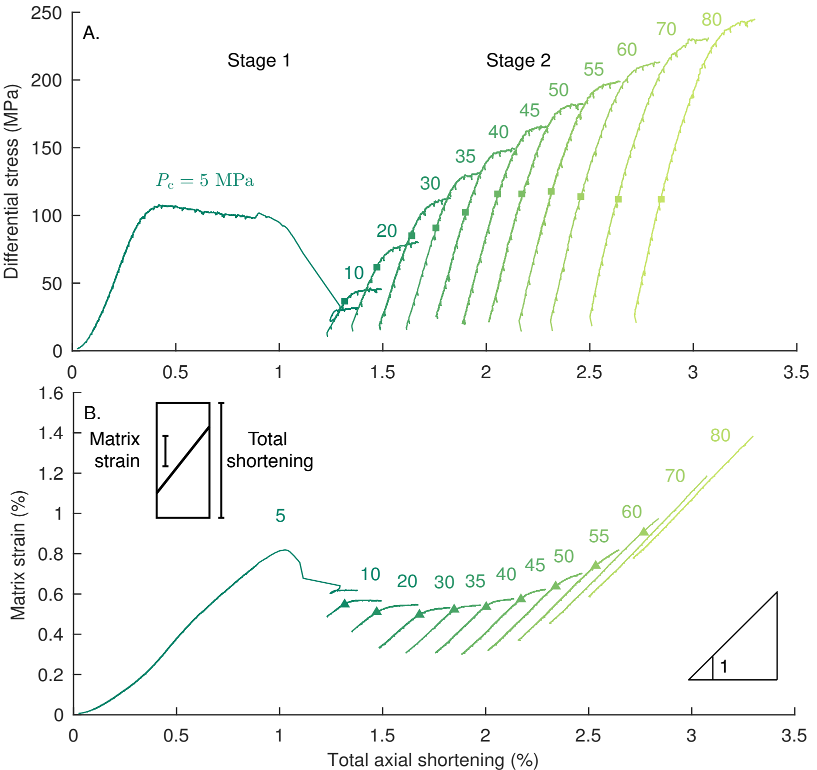
A.
Stage 1
Stage 2
Differential stress (MPa)
0
50
100
150
200
250
$P_\mathrm{c} = 5$ MPa
10
20
30
35
40
45
50
55
60
70
80
0
0.5
1
1.5
2
2.5
3
3.5
B.
Matrix strain
Total shortening
Matrix strain (%)
0
0.2
0.4
0.6
0.8
1
1.2
1.4
1.6
5
10
20
30
35
40
45
50
55
60
70
80
1
0
0.5
1
1.5
2
2.5
3
3.5
Total axial shortening (%)

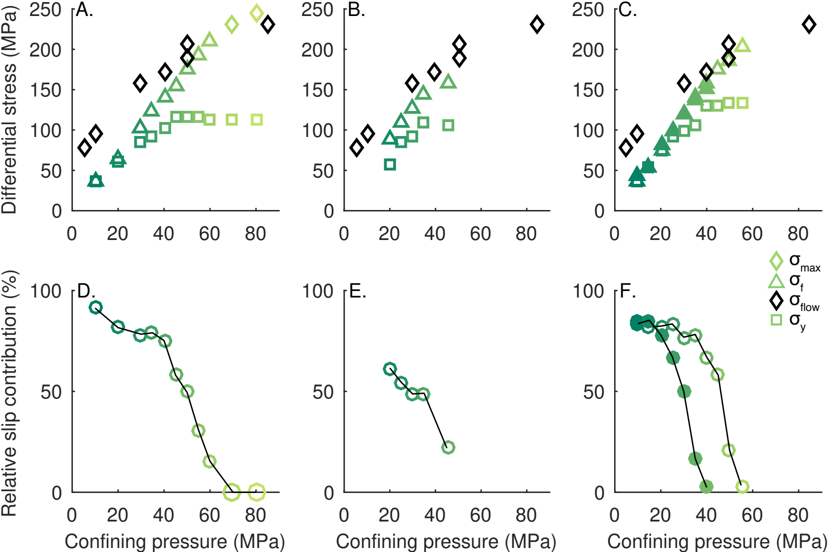
A.
B.
C.
D.
E.
F.
Differential stress (MPa)
0
50
100
150
200
250
Relative slip contribution (%)
0
50
100
Confining pressure (MPa)
0
20
40
60
80
σ_{max}
σ_f
σ_{flow}
σ_y

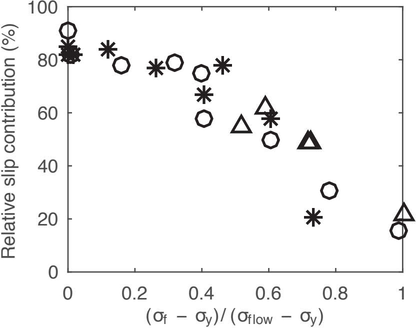
Relative slip contribution (%)
100
80
60
40
20
0
0
0.2
0.4
0.6
0.8
1
(σf − σy)/(σflow − σy)

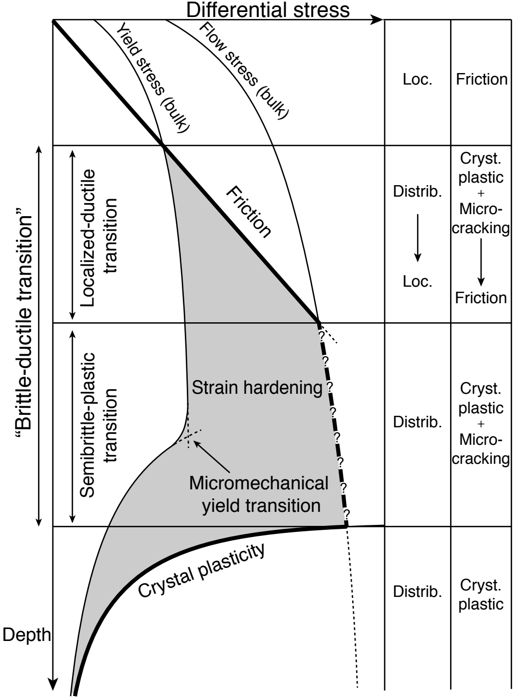
Differential stress
Yield stress (bulk)
Flow stress (bulk)
Loc.
Friction
"Brittle-ductile transition"
Localized-ductile transition
Friction
Distrib.
Loc.
Cryst. plastic + Micro-cracking
Friction
Semibrittle-plastic transition
Strain hardening
Micromechanical yield transition
Distrib.
Cryst. plastic + Micro-cracking
Crystal plasticity
Distrib.
Cryst. plastic
Depth
?